Available online at www.sciencedirect.com

SciVerse ScienceDirect

Scripta Materialia 68 (2013) 647–650

Scripta MATERIALIA

www.elsevier.com/locate/scriptamat

Coherent nanoscale ternary precipitates in crystallized $Ca_4Mg_{72}Zn_{24}$ metallic glass

Y.N. Zhang,[a] X.D. Liu,[b] Z. Altounian[b] and M. Medraj[a,*]

[a] *Department of Mechanical Engineering, Concordia University, 1455 de Maisonneuve Blvd. W., Montreal, Quebec, Canada H3G 1M8*
[b] *Center for the Physics of Materials and the Department of Physics, McGill University, 3600 University Street, Montreal, Quebec, Canada H3A 2T8*

Received 13 November 2012; revised 22 December 2012; accepted 24 December 2012
Available online 3 January 2013

The ternary precipitates in the $Ca_4Mg_{72}Zn_{24}$ metallic glass formed during heat treatment were characterized by differential scanning calorimetry, X-ray diffraction and transmission electron microscopy (TEM). The melt-spun sample after heat treatment exhibits nanoscale elongated precipitates of $Ca_2Mg_5Zn_{13}$ distributed at the grain boundaries and plate-like precipitates of $Ca_2Mg_6Zn_3$ in the grain interior of the Mg matrix. Both of these ternary compounds were identified by high-resolution TEM as precipitates that were coherent with the Mg matrix and could result in enhanced mechanical properties.

Keywords: Ca–Mg–Zn system; Magnesium alloys; Metallic glass; Ternary precipitates; TEM

Mg-based alloys have great potential for high-performance aerospace and automotive applications owing to their low density, high fuel efficiency, excellent castability and good machinability. However, their limited strength and low corrosion resistance are major shortcomings [1,2]. Mg–Zn is one of the most promising systems, possessing moderate strength, corrosion resistance and age-hardening response due to the formation of stable and metastable phases, such as $Mg_{51}Zn_{20}$, MgZn (or $Mg_{12}Zn_{13}$), Mg_2Zn_3 and $MgZn_2$ [3–8]. Addition of Ca up to 0.3 wt.% was reported to increase ductility through grain size refinement [9]. The Ca content in Mg alloys improves strength, castability, and creep and corrosion resistance [2]. In addition, Zn and Ca together with Mg form $Ca_2Mg_6Zn_3$, which is more stable than Mg_2Ca binary compound at lower temperatures (<623 K). $Ca_2Mg_6Zn_3$ is responsible for the age-hardening behavior and further enhances the strength and creep resistance of Mg-based alloys [10–14]. Recently, Mg-rich Ca–Mg–Zn biocompatible metallic glass containing small amounts of Ca (0–8 at.%) has been found to be suitable for the development of biodegradable implants [15–17]. However, size effects, including grain sizes, can play an important role in age-hardening behavior, mechanical properties and biomedical applications [14,18–20]. To refine the microstructure of Ca–Mg–Zn alloys, we need to study the equilibrium, non-equilibrium phases and their phase relationships.

To date, the Ca–Mg–Zn isothermal section at 608 K was constructed using a combination of the high-throughput diffusion couple technique and equilibrated key alloys [21]. While many researchers have studied the hexagonal $Ca_2Mg_6Zn_3$ compound, the results are contradictory [14,22–25]. Recently, we reported on the solubility ranges and crystal structures of $Ca_2Mg_6Zn_3$ (IM1, IM denotes intermetallic compound) and another ternary solid solution $Ca_2Mg_5Zn_{13}$ (IM3) at 608 K using scanning electron microscopy (SEM), electron probe microanalysis (EPMA), transmission electron microscopy (TEM), electron back-scattered diffraction (EBSD) and X-ray diffraction (XRD) results [26,27]. The $Ca_2Mg_6Zn_3$ (IM1) and $Ca_2Mg_5Zn_{13}$ (IM3) hexagonal ternary compounds were found to be in equilibrium with the hexagonal close-packed Mg matrix [21] and can contribute to the age-hardening response. Recently, we have reported the crystallization characteristics of metallic glasses in the composition range of $Ca_4Mg_{72-x}Zn_{24+x}$ ($x = 0$ to 12, $\Delta x = 2$) studied through differential scanning calorimetry (DSC), XRD and the temperature dependence of electrical resistance [28]. In this work, to complement these efforts, a combination of rapid solidification and heat treatment was used to achieve a decrease in the grain size, the formation of stabilized

* Corresponding author; E-mail: mmedraj@encs.concordia.ca

1359-6462/$ - see front matter
http://dx.doi.org/10.1016/j.scriptamat.2012.12.028

equilibrium phases, refinement of intermetallic particle sizes, and modification of the morphologies of the Ca–Mg–Zn alloy.

Samples with the nominal composition $Ca_4Mg_{72}Zn_{24}$ (at.%) were prepared in an arc-melting furnace with a water-cooled copper crucible in an argon atmosphere using a non-consumable tungsten electrode. The starting metals were supplied by Alfa Aesar with purities of 99.98% Mg, 99.99% Zn and 99% Ca. Samples were re-melted five times to ensure homogeneity. To compensate for the mass loss of Mg and Zn due to their high vapor pressure, an extra 8 and 12 wt.% of Mg and Zn, respectively, were added to the compositions before melting. The sample was then crushed into an appropriate size for single-roller melt-spinning. The melt-spinning was carried out under helium at a pressure of 50 kPa with a wheel tangential speed of 30 m s^{-1}. The resulting ribbons were approximately 2 mm wide and 30 μm thick. The actual composition of the ribbon samples was determined to be $Ca_4Mg_{76}Zn_{20}$ (at.%) using inductively coupled plasma spectroscopy and SEM. The difference between these two measurements is ±0.5 at.% on average.

XRD was firstly used to verify the amorphous state on the free side of each ribbon and to characterize the sample after each exothermic crystallization peak. The XRD patterns were obtained using a PANalytical X'pert Pro powder X-ray diffractometer with a Cu K_α radiation at 45 kV and 40 mA. The XRD spectrum was acquired from 20° to 120° 2θ with a 0.02° step size

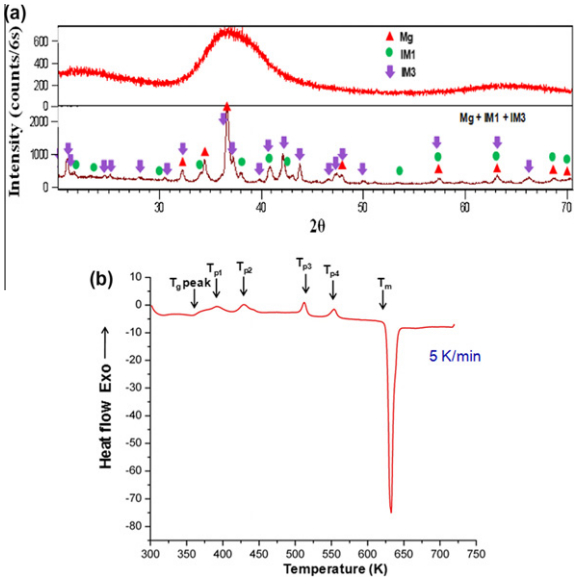

Figure 1. (a) XRD patterns of $Ca_4Mg_{72}Zn_{24}$ both as-quenched and heated beyond the final crystallization event. (b) DSC curve measured at a constant heating rate of 5 K min^{-1} showing the glass transition, crystallization and melting behavior of the $Ca_4Mg_{72}Zn_{24}$ metallic glass.

with a scan time 2 s per point. Analysis of the X-ray patterns was carried out using X'Pert HighScore Plus Rietveld analysis software in combination with Pearson's crystal database [29]. The thermal stability, glass transition and crystallization temperatures of the as-quenched glassy samples were studied by means of calibrated non-isothermal SETARAM differential scanning calorimeter under a continuous flow of purified argon. The samples were placed in a graphite crucible, covered with a lid and quickly cooled after the last exothermic peak to room temperature by flowing argon. The heat-treated samples were then investigated by XRD and TEM to determine the phases forming after the final crystallization event. Thin specimens for TEM observations were prepared by ion beam milling in a Gatan PIPS Model 691 at 3–5 kV from both sides of the ribbon. A Philips CM200 transmission electron microscope operated at 200 kV was used to characterize the specimens.

The XRD pattern obtained from the free side of the as-quenched sample is shown on the upper part of Figure 1a. The absence of detectable crystalline diffraction peaks, together with a broad scattering of signals around 37° and 67° 2θ, confirmed the amorphous nature of this sample. Figure 1b presents the DSC scan obtained at a constant heating rate of 5 K min^{-1} showing the glass transition, four crystallization events (marked by T_{p1}, T_{p2}, T_{p3} and T_{p4}) and the melting behavior. The XRD pattern for the sample heated to 583 K is shown in Figure 1a. From a Rietveld full pattern refinement, the crystallographic parameters and phase amounts of the refined phases for the last crystallization event are presented in Table 1. The atomic coordinates and site occupancy of IM1 and IM3 were taken from our previous findings [26,27]. After heating beyond the fourth crystallization event (583 K), Mg, IM1 and IM3 phases formed, which is consistent with the Ca–Mg–Zn equilibrium phase diagram [21].

The phase type, structure, morphology and coherency with the Mg matrix of the precipitates were characterized by TEM. Figure 2 shows bright-field (BF) images of the melt-spun $Ca_4Mg_{72}Zn_{24}$ metallic glass sample, heated beyond the final crystallization event, taken from the $[2\bar{1}\bar{1}0]_{Mg}$ orientation. The images show fine grains of about 200–500 nm in size. Compared with the grain sizes (1–2 μm) obtained from the $Ca_{1.0}Mg_{96.7}Zn_{2.3}$ (at.%) alloy through melt spinning reported by Jardim [11], a significant improvement in the grain size refinement was achieved in this work.

Elongated precipitates ~500 nm in length were distributed at the grain boundaries of both prismatic and pyramidal planes. Some of those precipitates are located along the grain boundary as shown in Figure 2a and b. Nie and Muddle [30] reported that the multiple precipitates lying on both prismatic and pyrami-

Table 1. The crystallographic parameters and phase amount of the refined phases forming after the final crystallization event of $Ca_4Mg_{72}Zn_{34}$.

Peak No.	Phases identified by XRD	Unit cell parameters			Phase amount (wt.%)
		a (Å)	*b* (Å)	*c* (Å)	
P4 (final crystallization event)	Mg	3.206	3.206	5.207	61.6
	$Ca_2Mg_6Zn_3$ (IM1)	9.475	9.475	9.966	8.2
	$Ca_2Mg_5Zn_{13}$ (IM3)	14.742	14.742	8.779	30.2

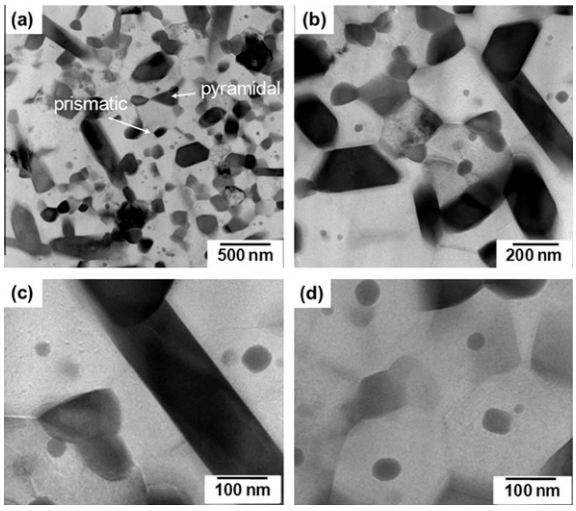

Figure 2. TEM images of the $Ca_4Mg_{72}Zn_{24}$ metallic glass heated beyond the final crystallization event at 583 K taken from the $[2\bar{1}\bar{1}0]_{Mg}$ orientation: (a) overview micrograph; (b–d) with increased magnification.

dal planes improve the mechanical strength of Mg alloys. In addition, Oh-ishi et al. [14] observed similar elongated precipitates in the $Ca_{0.3}Mg_{98.1}Zn_{1.6}$ (at.%) alloy. According to them, the composition of this alloy is near the two-phase region consisting of α-Mg and $Ca_2Mg_6Zn_3$ (IM1) and the three-phase region consisting of α-Mg, $Ca_2Mg_6Zn_3$ (IM1) and Mg_2Ca in the Ca–Mg–Zn ternary phase diagram. Hence, they have identified these precipitates as Mg_2Ca and/or $Ca_2Mg_6Zn_3$. However, according to our recent research [21], this alloy is located in the three-phase region consisting of α-Mg, $Ca_2Mg_6Zn_3$ (IM1) and $Ca_2Mg_5Zn_{13}$ (IM3) and these precipitates should be $Ca_2Mg_5Zn_{13}$ (IM3) instead of the Mg_2Ca or $Ca_2Mg_6Zn_3$ compounds. The hexagonal structure of IM3 was also indexed and confirmed by means of selected-area electron diffraction (SAED) based on our previous crystallographic study [27]. The SAED patterns are shown in Figure 3. Figure 3c and f present the SAED patterns of location A in Figure 3a and location B in Figure 3d, respectively. Two types of crystallographic orientation relationships were found between the IM3 and the hexagonal close-packed Mg matrix. This is the first time that such a relationship has been observed. Figure 3c indicates $[2\bar{1}\bar{1}0]_{Mg}//[1\,1\,\bar{2}\,3]_{IM3}$ and Figure 3f indicates $[2\bar{1}\bar{1}0]_{Mg}//[1\bar{2}\bar{1}0]_{IM3}$. Furthermore, the IM3 ternary precipitate was identified as a coherent with the Mg matrix, as shown by high-resolution transmission electron microscopy (HRTEM) images (Fig. 4a and b). The mismatch parameter, δ, where $\delta = (d_{IM3} - d_{Mg})/d_{Mg}$ (d value presents lattice spacing), is close to 0, indicating a perfect coherency between the Mg matrix and these IM3 ternary precipitates. Another crystallographic orientation relationship between the IM3 and the Mg matrix was observed in Figure 4b: $[2\bar{1}\bar{1}0]_{Mg}//[2\bar{1}\bar{1}0]_{IM3}$, $(0\,1\,\bar{1}\,1)_{Mg}//(0\,5\,\bar{5}\,1)_{IM3}$. The values of the lattice parameters a and c as well as the lattice spacing d for IM3, obtained from the SAED patterns (Figs. 3 and 4a and b), show good consistency with the XRD results (Fig. 1). Both the morphology and coherency of these

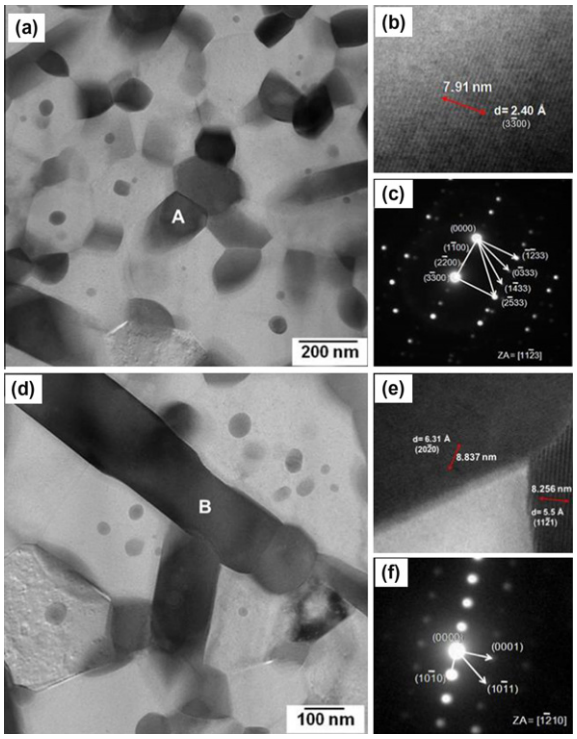

Figure 3. TEM images of the $Ca_4Mg_{72}Zn_{24}$ metallic glass beyond the final crystallization event at 583 K: (a, d) taken from the $[2\bar{1}\bar{1}0]_{Mg}$ orientation; (b, e) magnified pictures at the interface between nano-precipitated IM3 and Mg matrix; (c, f) SAED patterns for hexagonal IM3 ternary compound of the $[1\,1\,\bar{2}\,3]_{IM3}$ and $[1\bar{2}\,1\,0]_{IM3}$ orientations, respectively.

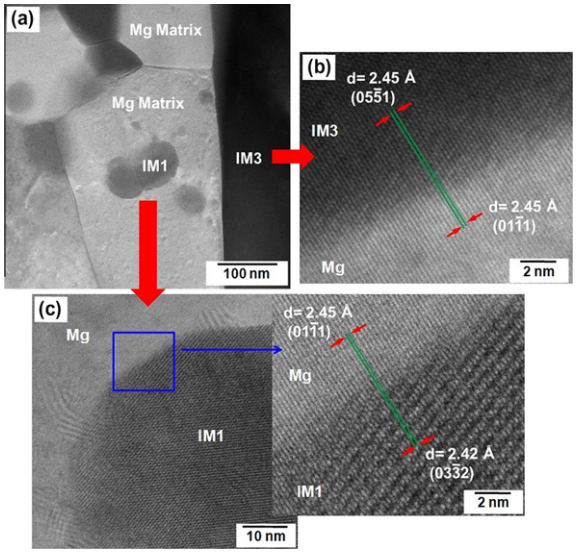

Figure 4. TEM images of the $Ca_4Mg_{72}Zn_{24}$ metallic glass beyond the final crystallization event at 583 K, taken from the $[2\bar{1}\bar{1}0]_{Mg}$ orientation: (a) overview; (b) HRTEM image of the interface between IM3 and Mg; (c) HRTEM image of the interface between IM1 and Mg.

elongated precipitates $Ca_2Mg_5Zn_{13}$ (IM3) distributed at the grain boundaries of the hexagonal close-packed Mg matrix are reported for the first time in this work.

In addition to the $Ca_2Mg_5Zn_{13}$ (IM3) elongated precipitates distributed at the grain boundary, fine dispersed plate-like hexagonal $Ca_2Mg_6Zn_3$ (IM1) precipitates were observed in the grain interior, as

shown in Figure 2. These $Ca_2Mg_6Zn_3$ (IM1) precipitates varied in size (20–100 nm) and shape (spherical and cuboid plate-like). The hexagonal structure of $Ca_2Mg_6Zn_3$ (IM1) was also indexed and confirmed by means of XRD results and HRTEM images, as shown in Figures 1 and 4c. As illustrated in Figure 4a and c, $Ca_2Mg_6Zn_3$ (IM1) ternary precipitate is also identified as coherent with the Mg matrix due to the very low mismatch δ (<2%) through HRTEM, as shown in Figure 4c. This shows a good consistency with the literature where the stable intermetallic compound $Ca_2Mg_6Zn_3$ has low lattice misfit with the Mg solid solution matrix [12,14] and proves the experimental accuracy of this work. The orientation relationships between the IM1 and the Mg matrix were observed as: $[2\bar{1}\bar{1}0]_{Mg}//[2\bar{1}\bar{1}0]_{IM1}$ $(0\bar{1}\bar{1}1)_{Mg}//(03\bar{3}2)_{IM1}$, as shown in Figure 4a and c. To summarize, these two types of precipitates forming within the matrix and at the grain boundaries of Mg matrix after the last crystallization event are $Ca_2Mg_6Zn_3$ (IM1) and $Ca_2Mg_5Zn_{13}$ (IM3) ternary compounds; this is confirmed by XRD and TEM results, and furthermore the composition of the sample is consistent with the phase relationship among Mg, IM1 and IM3 in the Ca–Mg–Zn phase diagram [21].

The ternary precipitates that form in $Ca_4Mg_{72}Zn_{24}$ metallic glass during heat treatment were characterized by DSC, XRD and TEM. A combination of rapid solidification and heat treatment was used to achieve refinement of the grains and intermetallic particle sizes, formation of the stable equilibrium ternary phases, modification of the morphologies, and verification of the orientation relationship between intermetallic particles and matrix. The heat-treated sample after the final crystallization event exhibited two types of precipitates and both of these ternary compounds were identified as equilibrium phases with the Mg matrix. The nanoscale spherical and cuboid plate-like precipitates $Ca_2Mg_6Zn_3$ (IM1) in the grain interior and the elongated precipitates $Ca_2Mg_5Zn_{13}$ (IM3) distributed at the grain boundary are coherent with the Mg matrix.

The authors would like to acknowledge Dr. X.B. Liu of the Physics Department of McGill University for useful discussions and suggestions.

[1] T.M. Pollock, Science 328 (2010) 986–987.
[2] A.A. Luo, Int. Mater. Rev. 49 (2004) 13–30.
[3] D.Y. Maeng, T.S. Kim, J.H. Lee, S.J. Hong, S.K. Seo, B.S. Chu, Scr. Mater. 43 (2000) 385–389.
[4] J. Buha, Mater. Sci. Technol. A 492 (2008) 11–19.
[5] J. Buha, Mater. Sci. Technol. A 491 (2008) 70–79.
[6] F. Nie, B.C. Muddle, Scr. Mater. 37 (1997) 1475–1481.
[7] T. Zhou, D. Chen, Z.H. Chen, J.H. Chen, J. Alloys Compd. 475 (2009) L1–L4.
[8] M. Aljarrah, M. Medraj, X. Wang, E. Essadiqi, G. Dénès, A. Muntasar, J. Alloys Compd. 438 (2007) 131–141.
[9] O. Beffort, Ch. Hausmann, in: K.U. Kainer (Ed.), Magnesium Alloys and their Applications, Wiley-VCH Verlag Gmbh & Co. KGaA, Weinheim, 2000, pp. 215–220.
[10] P.M. Jardim, G. Solorzano, J.B.V. Sande, Microsc. Microanal. 8 (2002) 487–496.
[11] P.M. Jardim, G. Solorzano, J.B.V. Sande, Mater. Sci. Technol. A 381 (2004) 196–205.
[12] G. Levi, S. Avraham, A. Zilberov, M. Bamberger, Acta Mater. 54 (2006) 523–530.
[13] M. Bamberger, G. Levi, J.B.V. Sande, Metall. Mater. Trans. A 37A (2006) 481–487.
[14] K. Oh-ishi, R. Watanabe, C.L. Mendis, K. Hono, Mater. Sci. Technol. A 526 (2009) 177–184.
[15] B. Zberg, P.J. Uggowitzer, J.F. Löffler, Nat. Mater. 8 (2009) 887–891.
[16] E. Ma, J. Xu, Nat. Mater. 8 (2009) 855–857.
[17] X.N. Gu, Y.F. Zheng, S.P. Zhong, T.F. Xi, J.Q. Wang, W.H. Wang, Biomaterials 31 (2010) 1093–1103.
[18] J.R. Greer, J.T.M.D. Hosson, Prog. Mater. Sci. 56 (2011) 654–724.
[19] D.C. Jang, J.R. Greer, Nat. Mater. 9 (2010) 215–219.
[20] J.-Y. Kim, D. Jang, J.R. Greer, Adv. Funct. Mater. 21 (2011) 4550–4554.
[21] Y.N. Zhang, D. Kevorkov, F. Bridier, M. Medraj, Sci. Technol. Adv. Mater. 12 (2011) 025003.
[22] R. Paris, Ministère de L'Air 45 (1934) 1–86.
[23] J.B. Clark, Trans. AIME 221 (1961) 644–645.
[24] J.B. Clark, Joint Committee on Powder Diffraction Standards (JCPDS) Card (1961), 12–0266.
[25] T.V. Larinova, W.W. Park, B.S. You, Scr. Mater. 45 (2001) 7–12.
[26] Y.N. Zhang, D. Kevorkov, J. Li, E. Essadiqi, M. Medraj, Intermetallics 18 (2010) 2402–2411.
[27] Y.N. Zhang, D. Kevorkov, X.D. Liu, F. Bridier, P. Chartrand, M. Medraj, J. Alloys Compd. 523 (2012) 75–82.
[28] Y.N. Zhang, G.J. Rocher, B. Briccoli, D. Kevorkov, X.B. Liu, Z. Altounian, M. Medraj, J. Alloys Compd. 552 (2013) 88–97.
[29] P. Villars, K. Cenzual, Pearson's Crystal Data (2010).
[30] J.F. Nie, B.C. Muddle, Magnesium Alloys and their Applications, Werkstoff-Informationsgesellschaft, Frankfurt Germany, 1998, pp. 229–234.